Field-based estimation of cation exchange capacity using induced polarization methods

Running Title: *Field-based estimation of CEC using IP methods*

Abstract

This study investigates the potential of field-based induced polarization (IP) methods to provide *in-situ* estimates of soil cation exchange capacity (CEC). CEC influences the fate of nutrients and pollutants in the subsurface. However, estimates of CEC require sampling and laboratory analysis, which can be costly, especially at large scales. Induced polarization (IP) methods offer an alternative approach for CEC estimation. The sensitivity of IP measurements to the surface properties of geological materials makes them more appropriate than geophysical methods that are sensitive to bulk electrical properties (e.g., DC resistivity and electromagnetic induction methods). Such abilities of IP are well demonstrated in the laboratory; however, applications are lacking in field studies. In this work the ability of IP to characterize CEC of floodplain soils is assessed by implementing a methodology that allows for direct comparison between IP and soil parameters. In one field, soil polarization and CEC exhibited the expected positive correlation; and multi-frequency measurements showed no clear advantage over single-frequency measurements. In another field, coarser soils (with low CEC) exhibited a high polarization. These coarser soils in the second field were characterized by anomalous magnetic susceptibility values, and hence the polarization was attributed to the presence of

magnetic minerals. Although better than order-of-magnitude estimates of CEC were possible in soils without substantial magnetic minerals, characterization of porosity, saturation, cementation and saturation exponents, and pore fluid conductivity would improve predictions. However, characterization of these parameters would require similar efforts as direct CEC measurements. This study contributes to bridging the gap between laboratory-derived relationships and their applicability in field applications. Overall, this work provides valuable insight for future studies seeking to understand polarization mechanisms in soils at the field scale.

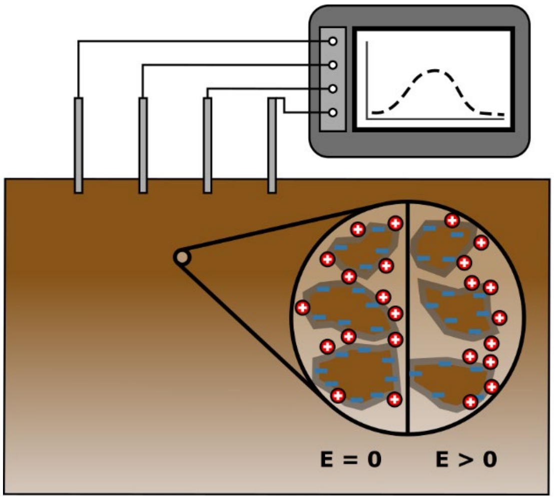

Graphical Abstract – Experimental design showing electrode layout and recorded spectral induced polarization (SIP) data. The left half of the zoomed in region shows the equilibrium state with no applied electrical field. The right half shows the situation whereby an electrical field causes the cations to migrate on the surface of mineral grains; which can then be measured with the SIP method.

Keywords: Induced Polarization, Hydrogeophysics, Petrophysics, Cation Exchange Capacity, Floodplains, Contamination

1. Introduction

The ability of the subsurface to retain and exchange cations has important implications for groundwater-surface water interactions (e.g., Smith and Lerner, 2008), agriculture (e.g., Ramos et al., 2018), and contaminant transport (e.g., Laing et al., 2009). For example, floodplain sediments can attenuate river-borne nutrients and contaminants to reduce ecological degradation (e.g., Overton et al., 2023). In agriculture, nutrient retention influences the leaching of fertilizers into groundwater (e.g., Gaines and Gaines, 1994; Abdelwaheb et al., 2019).

Attenuation characteristics of porous media are commonly quantified using cation exchange capacity (CEC), a parameter related, in part, to the electrically charged surfaces of porous media. Materials containing a high proportion of clay minerals and organic matter (OM) are characterized by high CEC values. However, measuring CEC is labor intensive and relies on laboratory analysis; this makes it difficult to characterize variability at the field scale. Consequently, there is substantial motivation to investigate methods that can make *in situ* assessments of CEC.

Geophysical methods offer a promising approach for estimating CEC in the field. They are relatively low-cost, quick to deploy, and have a larger measurement support volume than conventional soil sampling. Triantafilis et al. (2009) showed positive correlations between CEC and electrical conductivity measurements from frequency domain electromagnetic induction (EMI) measurements. Similarly, McLachlan et al. (2022) found that CEC covaried with the in-phase component of EMI measurements in vineyard soils. The in-phase component of EMI measurements is related to magnetic susceptibility, and consequently, the link between CEC and in-phase was attributed to the iron content in the soil, which was concentrated in areas with high OM and CEC. Importantly, although Triantafilis et al. (2009) attributed the high bulk electrical conductivity values to CEC, bulk electrical conductivity is also strongly dependent on water content (e.g., Archie, 1942). High CEC is typically associated with greater soil water retention (e.g., due to the finer texture), so CEC will often be positively correlated with water content. Therefore, relationships linking CEC and bulk electrical conductivity are likely to be ambiguous and site-specific.

Induced polarization (IP) methods offer an alternative approach for estimating CEC as they are sensitive to electrical polarization phenomena occurring at grain surfaces. Whereas bulk electrical conductivity is dominated by fluid content and fluid composition of the pore space, polarization is more closely related to the electrochemistry of grain surfaces (e.g., Kemna et al., 2012). Numerous laboratory studies have demonstrated strong links of IP with surface area, hydraulic conductivity, and CEC (e.g., Börner and Schön, 1991; Binley et al., 2005; Slater et al., 2007; Weller et al., 2010; Revil et al., 2012; 2014; Niu et al., 2016; Weller and Slater, 2019). Moreover, many of these works have demonstrated generalizable relationships that can be applied to large datasets comprising different, predominantly saturated, geological materials (e.g., Revil et al., 2017). However, despite the progress made in laboratory studies, successful field-scale demonstrations are comparatively rare.

The relative scarcity of field-based studies can be attributed to the complexities of field-based IP acquisition. For instance, it is easier to control important parameters, e.g., fluid saturation and pore-fluid electrical conductivity, in laboratory studies. Another key difference is that whereas laboratory studies typically focus on broad-spectrum multi-frequency measurements, this is generally not possible in the field. Consequently, the polarization behavior of materials tends to be better characterized in laboratory studies.

It is also simpler to directly compare IP measurements with parameters of interest. Given the small sample volumes typically analyzed in laboratory experiments, SIP measurements can be made at equivalent scales. As noted by Singha et al. (2015), discrepancies in scales have been a key obstacle in the petrophysical interpretation of field-based electrical resistivity data. Consequently, the principal aim of this work is to assess the ability of field-based IP methods to make quantitative estimates of CEC. However, before discussing specific objectives, it is important to consider aspects of the IP method in some detail.

2. Induced Polarization

2.1. Complex conductivity measurements

The following focuses on frequency domain IP measurements; for further background on IP, including time-domain IP, see Binley and Slater (2020). Frequency domain IP measurements are determined from the amplitude and phase shift of a measured voltage between two electrodes, relative to a current injected between another two electrodes. Measurements are typically expressed as complex conductivity, σ^*.

$$\sigma^*(\omega) = \sigma'(\omega) + i\sigma''(\omega), \tag{1}$$

where ω represents the frequency, σ' represents the real component of electrical conductivity and σ'' represents the imaginary component. At low frequencies (e.g., < 1 kHz), and the absence of matrix conductivity, the real component is typically described by current flow in pore fluids and at the grain-fluid interface (see Waxman and Smits, 1968):

$$\sigma' = \sigma_{el} + \sigma'_{surf}, \tag{2}$$

where σ_{el} and σ'_{surf} represent the electrolytic and real surface conductivity, respectively. In comparison, the imaginary component is typically described by phenomena occurring at the grain-fluid interface (see Vinegar and Waxman, 1984):

$$\sigma'' = \sigma''_{surf}, \tag{3}$$

The equivalence of σ'' and imaginary surface conductivity (σ''_{surf}) infers that the IP method provides a more direct route to CEC quantification than methods sensitive to bulk electrical conductivity (which is typically dominated by σ'), e.g., EMI or DC resistivity. However, it is important to note that σ'' is not independent from saturation and pore water conductivity. For instance, a decrease in saturation results in a decrease in the connectivity of the fluid-grain interface, and a change in pore water conductivity results in a change in the concentration of counterions at the grain-fluid interface (see Vinegar and Waxman, 1984; Weller and Slater, 2012).

Complex conductivity values are frequency-dependent; consequently, multi-frequency measurements are often used to characterize the spectral behavior of porous media. This approach is referred to as spectral IP (SIP) and in laboratory studies frequencies typically range from 1 mHz to 1 kHz. In comparison, field measurements typically have narrower bandwidths. For instance, Revil et al. (2021) collected usable data between 125 mHz and 37.5 Hz due to errors associated with electromagnetic inductive and capacitive effects. Similarly, Moser et al. (2023) collected data between 1 and 240 Hz but noted that data above 15 Hz were characterized by high measurement errors, again related to electromagnetic effects.

Electromagnetic effects are commonly encountered in field-based IP studies; consequently, there is a substantial body of work assessing approaches to improve the quality of IP data. In summary, electromagnetic capacitive effects occur due to high electrical resistance between electrodes and the ground, or due to the conductive shielding of the cables relative to the ground surface (e.g., Zimmermann et al., 2008; Zhao et al., 2013; Revil et al., 2021). In comparison, electromagnetic inductive effects are predominantly related to the current flow along the cables between electrodes and IP instruments. The magnitude of inductive effects is proportional to the cable length, the subsurface electrical properties, and the frequency of the injected current (e.g., Ingeman-Nielsen and Baumgartner, 2008; Schmutz et al., 2014; Flores Orozco et al., 2018). It should be noted that electromagnetic effects have also been observed in laboratory studies, however, approaches to account for these effects have been implemented, e.g., Wang et al. (2021a).

2.2. Relaxation Models

The frequency dependence of complex conductivity in laboratory studies is typically analyzed using phenomenological relaxation models (e.g., Cole and Cole, 1941; Pelton et al., 1978). Usage of these models is less common for field IP data because reliable model parameter fitting requires measurements across a broad frequency range. In this work the Pelton et al. (1978) model was used, see Tarasov and Titov (2013) and Slater and Weller (2022) for more background Cole-Cole and Pelton relaxation models. The Pelton model can be defined as follows:

$$\rho^*(\omega) \approx \rho_0(1 - M\left(1 - \frac{1}{1 + (i\omega\tau)^c}\right), \quad (4)$$

where ρ^* is the complex resistivity (the inverse of complex conductivity), ρ_0 is the low frequency, or DC, resistivity, M is the chargeability, c is the Cole-Cole exponent, and τ denotes the relaxation time. M is a measure of the integrated polarization strength, c can be considered to represent a range of polarization time scales, and τ represents an effective time constant of polarization (see Tarasov and Titov, 2013). These model parameters can be considered linked to the physical and electrochemical characteristics of the porous media. For example, finer-grain sediments are characterized by smaller τ values but a greater surface area and, thus, higher M values.

In petrophysical models, M is typically expressed as a normalized chargeability (i.e., $M_n = M/\rho_0$); M_n is recognized as a more direct measure of surface polarization (see Slater and Lesmes, 2002; Revil et al., 2017). It should also be noted that M_n can be obtained from the difference between high and low-frequency real conductivities (i.e., $M_n = \sigma'_\infty - \sigma'_0$). Additionally, given that field measurements typically have a limited bandwidth, M_n has been approximated from complex conductivity measurements made at two frequencies. For instance, Revil et al. (2017) proposed a relationship to obtain M_n estimates from two imaginary conductivity measurements for soils with broad of relaxation time distributions, i.e., no clearly defined peak in the σ'' spectra. These M_n approximations were subsequently used in the field study of Revil et al. (2021) who used IP tomography to estimate CEC in vineyard soils.

Often, the Pelton model (eq. 4) is expanded to include higher orders and account for high-frequency polarization effects (e.g., Maxwell-Wagner polarization and capacitive coupling). In this way, the low-frequency polarization effects, which are dictated by geological materials, can be resolved more accurately, see review by Kemna et al. (2012). The general equation for the multi-order Pelton model can be written as follows:

$$\rho^*(\omega) \approx \rho_0 \left(1 - \sum_{k=1}^{N} M_k \left(1 - \frac{1}{1+(i\omega\tau_k)^{c_k}}\right)\right). \qquad (5)$$

The difference between single and double Pelton models is highlighted in Figure 1. For the double Pelton model, σ'' continues to increase with frequency, whereas, for the single Pelton model, σ'' decreases at high frequencies. Importantly, in both spectra, the low-frequency parameters are identical. Consequently, if data are influenced by high-frequency effects, the low-frequency parameters will not be accurately determined by fitting a single-order relaxation model.

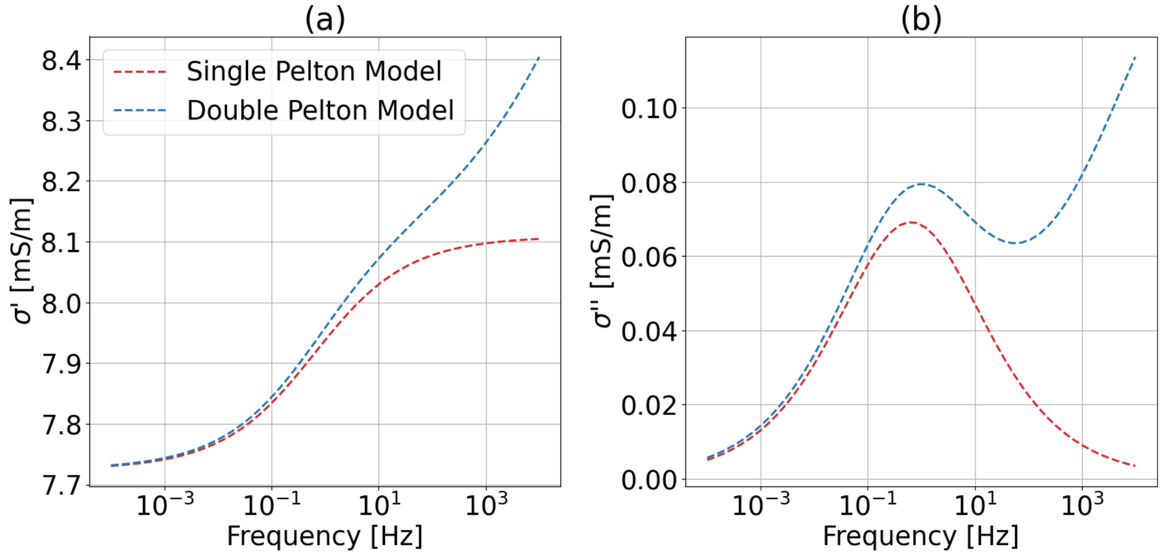

Figure 1: Single and double Pelton models for (a) real and (b) imaginary conductivity. The parameters used are as follows: ρ_0 = 130 ohm.m, M_1 = 0.05, τ_1 = 0.28 s, c_1 = 0.44, M_2 = 0.2, τ_2 = 1 x 10^{-6}s, c_2 = 0.3

2.3. Petrophysical Models

Electrical polarization is caused by the accumulation of ions and electrons on grain surfaces due to an external electrical field, see Kemna et al. (2012) and Revil et al., (2022). A substantial body of work has sought to explain polarization mechanisms via either mechanistic or empirical petrophysical models (e.g., Revil and Florsch, 2010; Jougnot et al., 2010; Weller and Slater, 2015; Revil et al., 2017). However, detailed consideration of this body of work is beyond the scope of this discussion. Instead, the focus is on the early empirical work of Vinegar and Waxman (1984) which is a precursor to much of the subsequent petrophysical literature. Vinegar and Waxman (1984) demonstrated that the Waxman and Smits (1968) model can be used to explain σ':

$$\sigma' = \frac{1}{F} S^n \left(\sigma_w + \frac{BQ_v}{S}\right), \tag{6}$$

where *F* is the Archie (1942) electrical formation factor, $F = \phi^{-m}$ (with ϕ and *m* representing the porosity and the cementation exponent, respectively), *S* is the water saturation, σ_w is the pore water electrical conductivity, *B* is the equivalent ionic conductance of clay exchange cations as a function of σ_w, and Q_v is the CEC normalized by pore volume. Importantly, whereas CEC values are typically expressed in meq/100 g, Q_v is expressed in meq/cm^3, consequently, transformations between both quantities would require knowledge of soil bulk density. Vinegar and Waxman (1984) also defined a relationship for σ'':

$$\sigma'' = \frac{1}{F_{im}} S^n \lambda Q_v, \tag{7}$$

where F_{im} is the formation factor for imaginary conductivity, ($F_{im} = \phi F = \phi^{1-m}$, for saturated conditions) and λ represents the apparent mobility of the counterions. Vinegar and Waxman (1984) noted that although *F* offers a good empirical fit for their data, using F_{im} provided an improved fit. Vinegar and Waxman (1984) reason that this is because σ'' has additional dependence on pore size; they propose that pore constrictions cause a membrane blockage effect and a displacement of clay counterions that is particularly dependent on water saturation.

To highlight the relationship between σ'' and CEC, several saturated datasets measured at Lancaster University (Lancaster, UK) are shown in Figure 2. The Accusand sample consisted of well-rounded, spherical 0.8 to 1.7 mm diameter sand grains and were obtained from Unimin Corporation (Minnesota, US). The Hanford sand samples were obtained at Pacific Northwest National Laboratory (Ward, pers. comm., 2010) and originated from the Hanford 300 site (Washington, US). The Binley et al. (2005) samples comprised medium and fine-grained fluvial sandstones from northern England, UK. The Mejus (2016) samples were a range of sandstones, sands, clays, and tills, also collected from northern England, UK. The Razavirad et al. (2019) samples comprised clean (clay-poor) sands and sandstones from the Persian Gulf, Iran. Lastly, the samples from McLachlan et al. (2020) comprised riverbed sands and gravels from northern England, UK.

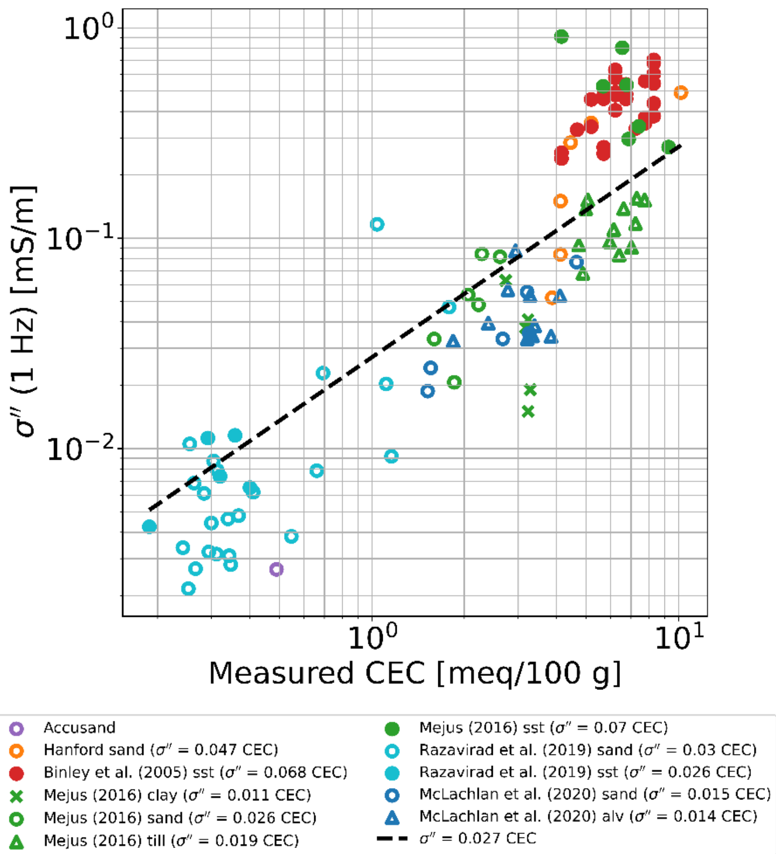

Figure 2: Imaginary conductivity and CEC measurements from datasets measured at Lancaster University (Lancaster, UK). The black dashed line represents the line of best fit (i.e., $\sigma'' = 0.027\,CEC$). Sst refers to sandstone samples.

In all cases, CEC measurements were made using the ammonium acetate approach (see Chapman, 1965), as discussed below in section 3.2.2. Most of the SIP measurements were made with 100 mS/m NaCl saturating solutions, however, the McLachlan et al. (2020) samples were saturated with a 58 mS/m NaCl solution to match water conductivity at the field site. To account for this, the McLachlan et al. (2020) σ'' values were adjusted following the procedure described in Weller and Slater (2012).

Given that the IP measurements were made on saturated samples, eq. 7 can be simplified as $\sigma'' = aCEC$, where *a* contains information related to pore fluid chemistry, mineralogy, and F_{im}. This simple linear relationship has the same form as an empirical model proposed by Weller et al. (2010) to link σ'' and pore-normalized surface area, S_{por} for a range of sand and sandstone samples. The $\sigma'' = 0.027\, CEC$ relationship fits the data in Figure 2 relatively well; the scatter can be attributed to differences in formation factors and mineralogy. For instance, the Binley et al. (2005) and Mejus (2015) sandstones are likely to be characterized by lower F_{im} than the other samples; furthermore, formation factor variability could also explain within-dataset variability in σ''.

In addition to relationships linking σ'' and CEC (e.g., Vinegar and Waxman, 1984; Revil et al., 2021; 2022), there have been relationships proposed using chargeability. For instance, Revil et al. (2021) proposed a relationship linking M_n and CEC, where M_n is approximated from high and low frequency imaginary conductivity measurements (see Revil 2017). They define the relationship as follows:

$$M_n = \theta^{m-1}\rho_g \lambda CEC \tag{8}$$

where θ is the volumetric water content, ρ_g is the grain density, λ represents the apparent mobility of the counterions (as also used in eq. 7). Equation 8 is derived from relationships linking σ_∞ and σ_0 with CEC for partially saturated sediments, and it assumes that exponents *m* and *n* are both approximately equal to 2. More details are presented in Revil et al. (2021) and preceding work (i.e., Revil, 2012; Revil et al. 2013a; 2013b). Importantly, it should also be noted that Revil et al. (2021) estimate θ from M_n; thus, the accuracy of their CEC predictions is highly dependent on their approximated M_n values.

2.4. This Study

The primary objective of this work is to assess the ability of field-based IP methods to obtain *in situ* estimates of CEC in the unsaturated zone. This objective requires that high-quality SIP data are collected. To this end, a field setup that mitigates many of the issues encountered in the field was designed. The approach involved collecting SIP measurements with a single quadrupole and short coaxial cables to mitigate electromagnetic errors often seen in larger-scale IP studies (e.g., Schmutz et al., 2014; Moser et al., 2023).

Additionally, by using a small electrode spacing, the depth of investigation was relatively shallow. This approach made it easier to collect representative soil measurements and make direct comparisons between measured and predicted CEC values. It should be highlighted that, although technically feasible to conduct, imaging-type measurements using multiple electrode arrays were avoided. Instead, the work focuses on assessing the links between CEC and SIP parameters and thus avoiding the influence of imaging artefacts, for example, is critical. If reliable links between CEC and SIP can be established, then they could be used in future IP imaging.

This work focuses on three primary goals:

1. Assessing the advantages of multi-frequency over single-frequency polarization measurements.
2. Determining the importance of other soil parameters in polarization.
3. Evaluating the ability of field-based IP measurements to provide quantitative estimates of CEC.

In this work, two petrophysical relationships are used to link polarizability to CEC: one uses σ'', and the other uses M_n from a double Pelton model fitting. The first is derived from Vinegar and Waxman (1984) and uses a fitting coefficient, b_{im}:

$$\sigma'' = b_{im}\phi^{m-1}S^{n}CEC. \tag{9}$$

The second equation has a similar form but links M_n and *CEC* with the fitting coefficient, b_{Mn}:

$$M_n = b_{Mn}\phi^{m-1}S^n CEC. \quad (10)$$

In both cases, the fitting coefficients contain information about the pore water conductivity, counterion mobility, and bulk density. For instance, eq. 9 is comparable to eq. 7, as defined by Vinegar and Waxman (1984), and eq. 10 is comparable to eq. 8, as defined by Revil et al. (2021).

The first goal assesses the benefit of multi-frequency IP over single-frequency IP. As noted, polarization can be assessed from σ'' measurements (i.e., single frequency measurements) or M_n measurements, which require broadband SIP measurements. Given the difficulties in collecting high-frequency IP data in the field and their importance in accurately determining M_n, there is a clear rationale for assessing the value of collecting multi-frequency measurements. Moreover, given the time required for low-frequency measurements, collecting single-frequency, or time-domain, data has the added benefit of reducing acquisition times in the field significantly.

The second goal investigates the importance of other soil parameters in influencing polarization behavior. For instance, in addition to CEC, polarization is also dependent on water content, porosity, mineralogy, and cementation and saturation exponents. To this end, measurements of texture, water content, and magnetic susceptibility (as a proxy for mineralogy) were collected. In comparison, cementation and saturation exponents were assumed homogenous, as discussed in section 3.3. Importantly these assumptions will also influence the fitting coefficients in eq. 9 and 10.

The last goal is to evaluate the ability of field-based IP to provide quantitative estimates of CEC using eq. 9 and 10. This goal seeks to determine if the large-scale relationships observed for multiple data sets (e.g., Figure 2) are meaningful for quantitatively assessing CEC variability at the field scale.

3. Materials and Methods

3.1. Study Site

The study site is in the catchment of the River Conder, Lancaster, UK (Figure 3). The land is owned by Lancaster University and is managed as farmland, grassland, and woodland. Two study fields adjacent to the river were selected, hereafter referred to as the North Field and the South Field, both of which are periodically flooded. The North Field is used for cattle grazing, and the South Field is used for silage production and has no permanent livestock. The bedrock in the area comprises Carboniferous mudstones, siltstones, and sandstones; the superficial cover comprises glacial tills and fluvial deposits of clay, silt, sand, and gravel.

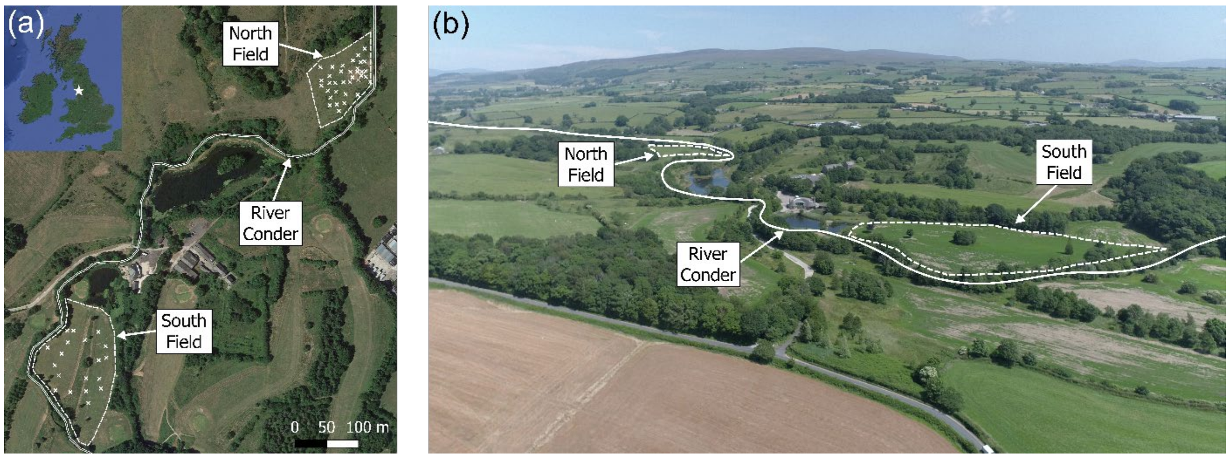

Figure 3: (a) map of the field site with locations of field measurements, and (b) aerial image of the field site.

3.2. Field Measurements

The field measurements were conducted on several campaigns. The bulk of the work was completed in five days (20 & 21-Nov-2021; 25-Apr-2022; 12 & 17-May-2022); on each day, co-located SIP measurements and soil samples were obtained alongside soil temperature and volumetric moisture content (VMC) measurements. As discussed below, the soil samples were subsequently analyzed for gravimetric water content (GMC), texture, and magnetic susceptibility (MS). CEC measurements were made on the samples collected on 25-Apr-2022, and 12 & 17 May 2022. Additional field campaigns were also conducted to collect soil samples to deeper depths, i.e., up to 2 m, (01-Apr-2022; 24-May-2022) and to obtain additional shallow samples to obtain porosity measurements and OM (11-Oct-2022).

3.2.1. Co-located SIP measurements and soil sampling

Soil samples were collected immediately after the SIP measurements to ensure that the SIP data were representative of the soil conditions. The SIP measurements were made using a PSIP instrument (Ontash and Ermac, New Jersey, US) and coaxial cables were used to mitigate electromagnetic errors. Although primarily designed for laboratory measurements, the instrument has been successfully used in field experiments previously. For example, Wang et al. (2021b) used the instrument to characterize the σ^* of riverbed sediments.

In the present work, data were collected using a Wenner configuration with 25 cm electrode spacing, whereby current is injected between the two outermost electrodes and the result voltage was measurement on the central electrode pair. The sensitivity profile (Figure 4a) shows that most of the sensitivity (i.e., ~90%) is focused in the upper 30 cm of the subsurface.

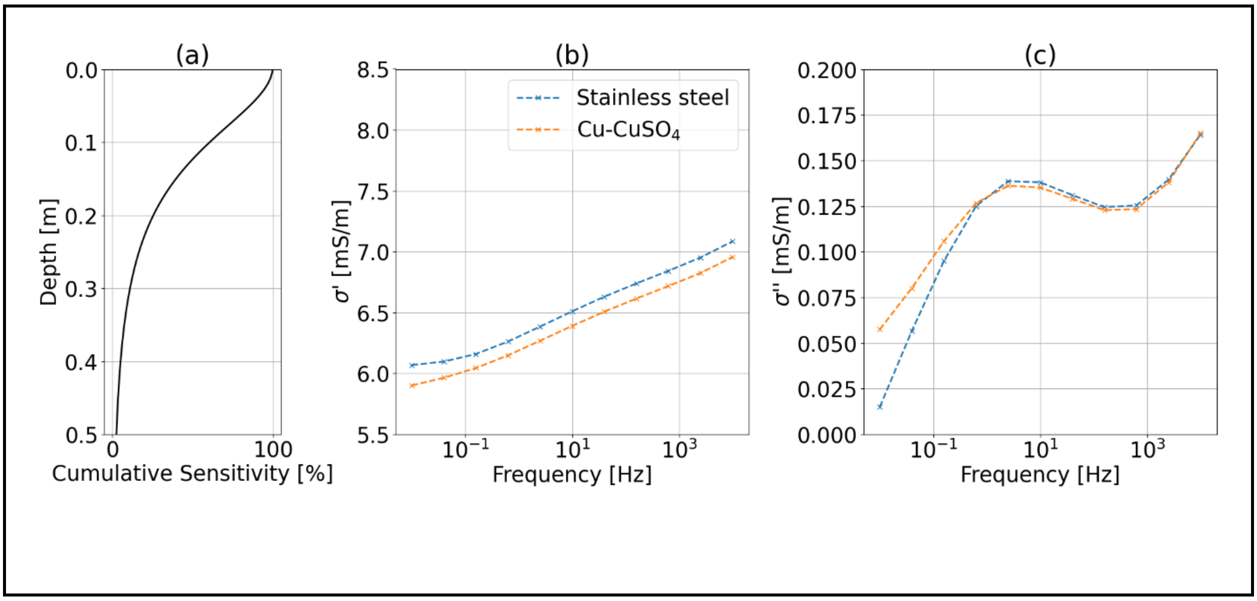

Figure 4: (a) cumulative sensitivity profile, (b) influence of electrode material on real conductivity, (c) influence of electrode material on imaginary conductivity.

Additionally, although several authors have advocated for using non-polarizable electrodes (e.g., porous pot electrodes) over stainless-steel electrodes, they require settling time and are therefore less practical. The importance of electrode type was assessed with some initial tests using both stainless-steel and Cu-$CuSO_4$ voltage electrodes (see Figures 4b and c). It can be observed that the σ' measurements are slightly higher for the measurements made with the stainless-steel current electrodes. This increase in σ' can be attributed to the electrodes influencing the subsurface conductivity given that they were inserted 2.5 cm into the ground, i.e., 10% of the electrode spacing. For σ'' beyond 0.3 Hz, there is good agreement between both electrode types. However, below 0.3 Hz, the stainless-steel electrodes measure lower σ'' values. Nonetheless, given the substantial increase in productivity, stainless-steel electrodes were used in this work.

SIP measurements were made at 13 logarithmically spaced intervals between 10 mHz and 10 kHz. After each SIP measurement, soil samples were collected using a hand auger to depths of 30 cm and bagged in 10 cm intervals. Three replicates were obtained at each location: at the midpoint of each electrode pair. Additionally, after each SIP measurement, temperature, and VMC measurements were made at 0 cm and 15 cm depths using a HI-98509 meter (Hanna Instruments, Leighton Buzzard, UK) and a ThetaProbe (Delta T Devices, Cambridge, UK), respectively, again at three locations. Although the sampling intervals for the soil samples, and the VMC and temperature measurements were different, the interest in this work is regarding the correlation of SIP with the bulk properties of the upper ~30 cm of the soil profile. Consequently, as discussed in 3.2.4., properties were averaged to obtain single values for the parameters of interest.

3.2.2. Laboratory soil measurements

GMC measurements were made on each sample within the week following sampling (in each case samples were stored in sealed bags and refrigerated before analysis). In each case, samples were dried for at least 48 hours at 105°C. Samples from the same depth interval for each measurement site were then homogenized before CEC, textural, and MS analyses.

CEC measurements were made using the ammonium acetate method (see Chapman, 1965). In each case, approximately 4 g of dry soil samples were centrifuged with sodium acetate solution to replace all cation sites with sodium ions. Methylated spirits were then used to remove non-bound sodium ions before ammonium acetate was used to displace the sorbed sodium. The amount of displaced sodium was then determined using a flame photometer (Model 410, Corning, AZ, US).

Textural analyses were done using a laser diffractometer (Beckman and Coulter, Brea, CA, US). First, samples were sieved to < 2 mm, and organic matter was removed using hydrogen peroxide. Samples were then homogenized before 1 g of sample was added to the laser diffractometer and run until the grain size distribution readings were stable (approximately 2 minutes).

The MS2 meter (Bartington Instruments, Witney, UK) was used to measure the bulk MS of 10 to 15 g of oven-dried soil in 10 cm^3 plastic pots. The device's dual frequency MS2B sensor (0.465 kHz and 4.65 kHz) was used to determine both the low and high-frequency mass-specific MS (χ_{LF} and χ_{HF}, respectively) in m^3/kg. Given that many of the samples were weakly magnetic, instrumental drift needed to be accounted for, especially for the higher frequency measurements. This correction was done using the 4-measurement-cycles procedure that corrects the sample reading with an air reading (see p. 44-45 in Dearing, 1999). The sample readings were also corrected for the diamagnetic signal of the plastic pot. The χ_{LF} and χ_{HF} values then allowed the calculation of the percentage of frequency-dependent susceptibility, $\chi_{FD}\%$:

$$\chi_{FD}\% = \frac{\chi_{LF} - \chi_{HF}}{\chi_{LF}} \times 100 \tag{11}$$

3.2.3. Additional soil sampling

The deeper-depth soil cores were collected to depths of 2 m using a Cobra TT percussion auger (Royal Eijkelkamp, Giesbeek, Netherlands). A total of 12 cores, 6 in each field, were collected and subsampled into 15 cm intervals. During the drilling, the samples were compacted; consequently, a compression factor was calculated for the entire core and used to rescale the core length. The gravel (i.e., grains exceeding 2 mm) content by dry mass of these cores was then determined for each interval.

Additional samples were also collected to make measurements of porosity and OM. A 5.25 cm diameter, 4 cm long PVC tube was pushed into the subsurface at depths of 0 and 15 cm. Samples were saturated in a water bath for 48 hours and weighed. The samples were dried in a 105°C oven and weighed again to determine porosity. The samples were then placed in a 505°C furnace for 24 hours to quantify the OM content.

3.2.4. Averaging of soil parameters

Given the small volume of the samples typically measured in laboratory-based SIP studies, the samples are typically assumed homogenous, and representative parameter values can be determined easily. In contrast, when field IP data are collected, they are typically modeled to get spatial distributions of σ' and σ''. Transformations of SIP data to depth-specific σ^* models are not possible for single quadrupole measurements.

Consequently, this work used an approach to weight the soil measurements by the sensitivity profile shown in Fig. 4a.

The relative sensitivities for each sampling interval were used to weight the soil parameters. For instance, the soil samples collected at the 0 – 10, 10 – 20, and 20 – 30 cm intervals were weighted with factors of 0.403, 0.335, and 0.262, respectively. In comparison, measurements made in the 0 – 15 and 15 – 30 cm intervals were weighted with factors 0.6 and 0.4, respectively. This approach is comparable to the 'apparent water content' approach used by Martini et al. (2018), whereby EMI sensitivity patterns are used to scale volumetric soil water contents.

3.3. Modeling SIP data

A double Pelton model (eq. 5) was fitted to the measured SIP spectra to obtain *M* and ρ_0 values, these where then used to compute M_n. The following objective function was used to determine the optimal Pelton model parameters:

$$\varphi = \frac{1}{2N}\sum_{i=1}^{N}\left(\left|\frac{\sigma'_{o,i} - \sigma'_{m,i}}{\sigma'_{o,i}}\right| + \left|\frac{\sigma''_{o,i} - \sigma''_{m,i}}{\sigma''_{o,i}}\right|\right) \quad (12)$$

where *N* is the number of frequencies, and σ'_o, σ'_m, σ''_o, and σ''_m represent the modeled and observed real and imaginary conductivities, respectively.

For the petrophysical modeling, the measured 1 Hz σ'' was used for eq. 9 and Pelton-defined M_n was used for eq. 10. For each measurement site, independent sensitivity weighted VMC and CEC values were used. However, given that porosity measurements were obtained at different sampling locations, an average sensitivity-weighted porosity value for each field was defined.

Additionally, the saturation and cementation exponents were both assumed to be 2 (e.g., Glover, 2015). The respective fitting coefficients, b_{im} and b_{Mn}, were determined by minimizing the root mean square error (RMSE) between predicted and observed CEC values. Although the saturation and cementation exponents could be determined alongside the fitting coefficients, they would be make highly correlated with b_{im} (eq. 9) and b_{Mn} (eq. 10).

4. Results

4.1. Deep Soil Auger Core

The North Field has a gravel-dominated horizon at depths of around 1.5 m to 2 m (Figure 4c-h). It appears that this horizon deepens towards the south of the North Field. Additionally, shallower gravel horizons can be seen at depths between 0.2 and 1.2 m, particularly in cores N1 and N2. In the South Field, there are gravel-dominated horizons at depths between around 1 m and 2 m (Figure 4i-n); however shallower gravel horizons are also present (e.g., S5 and S6). The gravel-dominated horizons are remnants of the meandering River Conder and indicate a dynamic depositional system. Given that the gravel content is typically low in the upper 30 cm, it is not anticipated to influence the SIP data substantially and is consequently not considered further.

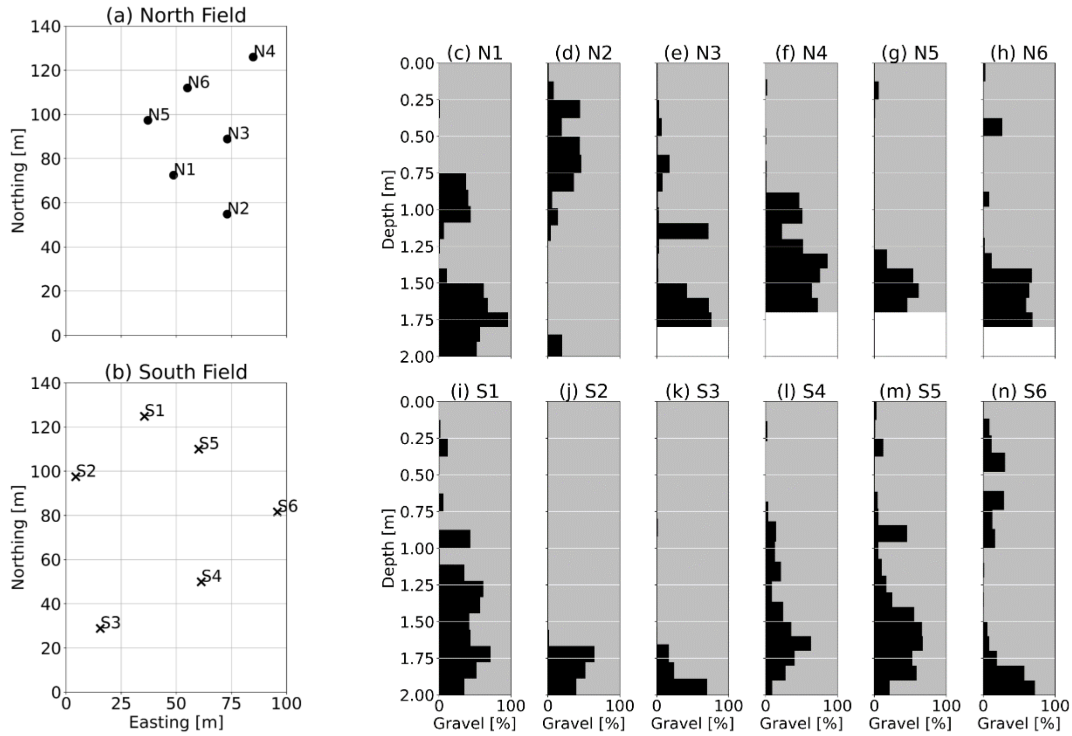

Figure 5: Location of deep core samples in (a) the North Field and (b) the South Field, (c-h) show the gravel cores from the North Field, and (i-n) show the gravel cores from the South Field.

4.2 CEC, water content, porosity, and OM

As expected, there is a strong correlation between the sensitivity averaged GMC and VMC in both fields (Figure 6). Moreover, although the data were collected on different days, both fields have a similar VMC range. However, it can be observed that GMC in the South Field is higher, for comparable VMC, i.e., the soil bulk density is higher. This can be attributed to different soil types in both fields, as evidenced by the predominantly lower sand content and higher CEC values in the South Field. Additionally, it can be observed in both fields that GMC content has a moderate positive correlation with CEC (Spearman's r = 0.71 for the North Field and 0.60 for the South Field); reasserting the earlier statement that relationships linking CEC and bulk electrical conductivity can be ambiguous given that saturation has a strong influence on real electrical conductivity.

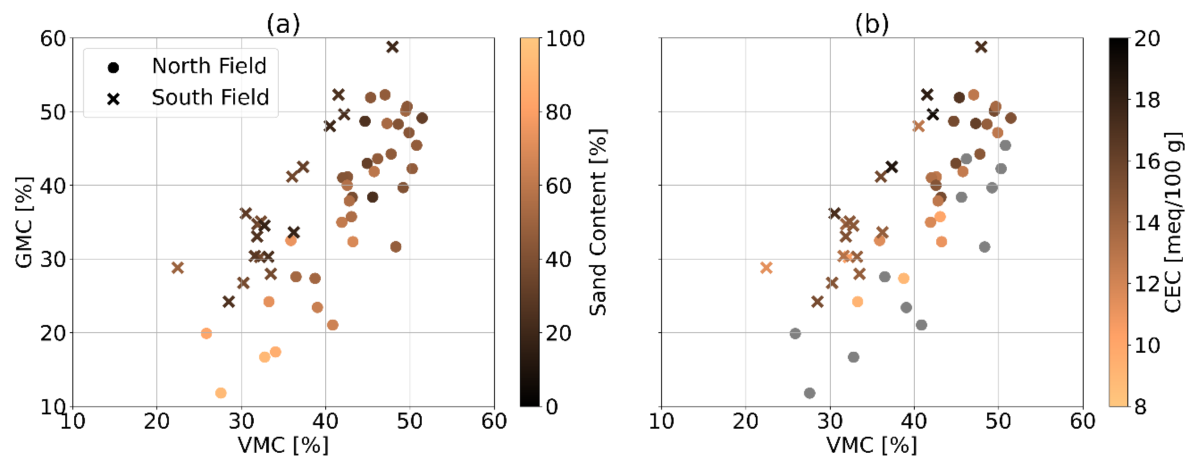

Figure 6: Gravimetric water content (GMC) and volumetric water content (VMC). (a) displays the points colored relative to their sand content, and (b) the points colored relative to their CEC. Grey colors indicate the sites where no CEC data were collected.

The spatial distributions of sensitivity-averaged sand, CEC, porosity, and OM are presented in Figure 7. In the North Field, there is a distinctive anomalous zone centered at an easting of 75 m and a northing of 85 m. This zone is characterized by high sand content and low CEC values. Although the sand content is relatively homogenous over the South Field, elevated CEC values can be observed in the north and the south of the field, Figure 7d. Given that there is a negligible correlation between CEC and clay content (*Spearman's r = -0.06*) and a moderate correlation between CEC and silt content (*Spearman's r = 0.54*), the elevated CEC in the north and south areas of the South Field can most likely be attributed to elevated OM content, see Figure 7d and h.

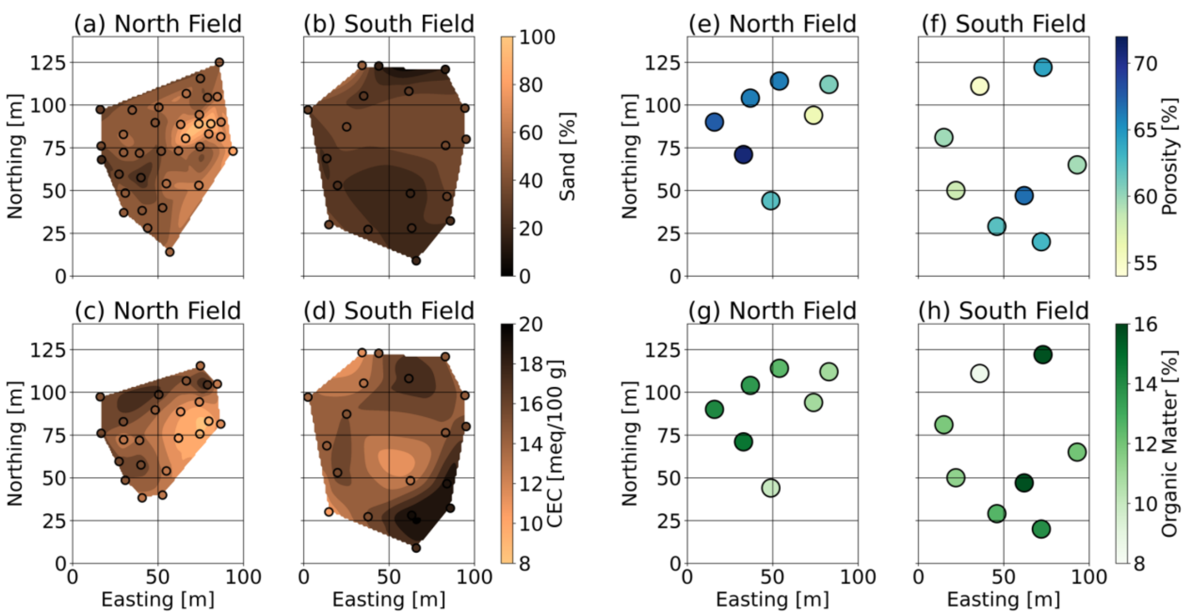

Figure 7: Maps of sand content in (a) the North Field and (b) the South Field, CEC in (c) the North Field and (d) the South Field, porosity in (e) the

North Field and (f) the South Field, and organic matter in (g) the North Field and (h) the South Field.

It can also be seen that the western portion of the North Field has the highest OM contents and the highest CEC values. However, it should be noted that in the North Field CEC has Spearman correlations of 0.57 and 0.66 with clay and silt, respectively, indicating that the CEC is more closely related to the fine content in the North Field (compared to the South Field). The porosity of the soils is higher in the North Field, i.e., 64.23 +/- 4.94% in comparison to 61.02 +/- 3.72% in the South Field, this is agreement with the South Field soils having higher bulk densities. Interestingly, the anomalous zone in the North Field is seemingly characterized by low porosity.

4.3 Magnetic Susceptibility

The spatial patterns in MS data from the 0 – 10 cm soil interval are presented in Figures 8a to d. The χ_{LF} values mostly range between 50 and 950 x 10^{-9} m^3/kg, which is typical for soils with weak to medium magnetic signatures. The relationship between frequency-dependent MS, $\chi_{FD}\%$, and χ_{LF} is shown for each interval in Figures 8e to g. Most of the samples show an increase in $\chi_{FD}\%$ with increasing χ_{LF} before $\chi_{FD}\%$ reaches a plateau at 9 – 10%. This pattern is indicative of natural soil formation on top of weakly magnetic parent material (see Dearing et al., 1996). For instance, *in situ* formation of ultrafine magnetite and maghemite grains can be expected in regularly flooded and well-drained soils (Grimley & Vepraskas, 2000; Grimley et al., 2008). This process increases both χ_{LF} and χ_{FD}%, see Maher (1988) and Dearing (1994) for further information.

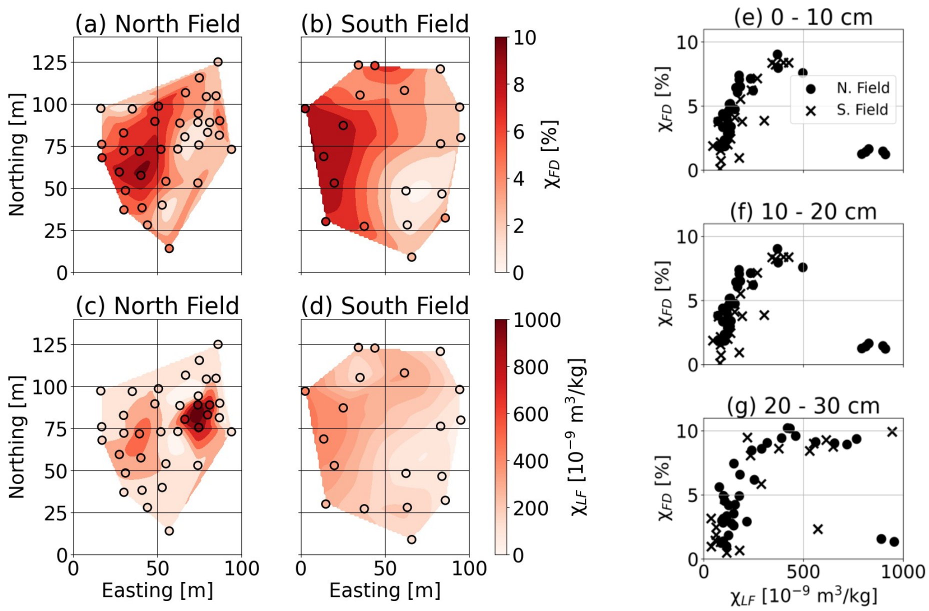

Figure 8: Maps of χ_{FD}% from 0 to 10 cm interval in the (a) North and (b) South Fields, χ_{LF} in the (c) North and (d) South Fields, (e) to (g) shows the χ_{LF} vs. χ_{FD}% for the 0 to 10 cm, 10 to 20 cm, and 20 to 30 cm intervals, respectively.

It can be observed that the anomalous zone in the North Field, as identified from the soil parameter maps (Figure 7), also exhibits anomalous MS values. The high χ_{LF} (500 to 1000 x 10^{-9} m^3/kg) and very low χ_{FD}% (typically between 1.5 and 2.0%) values of this zone indicate a more magnetic parent material than the other sites. In the first interval (0 to 10 cm), five samples from the North Field (sites NP2, NP7, NV7, NV8, and NH11) show this anomalous behavior, Figure 8e. In the second interval (10 to 20 cm), samples from the same five locations are also anomalous, Figure 8f. In the third interval (20 to 30 cm), one sample from the South Field (site SH5) and three samples from the North Field (sites NP2, NP7, and NV7) are anomalous, Figure 8g.

Soils from this zone in the North Field are characterized by elevated sand content (see Fig 7a), moreover many of the grains in the 1 – 2 mm range from these sites were black in color. Although potentially magnetic parent rocks (e.g., basaltic dykes and mudstones) are known in the area, the localized nature of this anomaly suggests human activity, i.e., imported sediments. For instance, it appears that sediments have been used in the eastern portion of the North Field to build an embankment and mitigate flooding from the river. More detailed investigations could focus on grain provenance or detailed magnetic studies (e.g., magnetite granulometry) to clarify the origin, however, these analyses are beyond the scope of this work.

4.4. SIP Results

To highlight the variability of the SIP measurements, two field days of data are presented, one in the North Field and one in the South Field (Figure 9). In general, the double Pelton model fitted the data well, root mean square percentage error (RMSPE) values for the σ' were typically below 1%, and RMSPE values for the σ'' typically ranged from 1 to 20%. However, it should be noted that RMSPE values of up to 72.8% were also observed for σ'', see Table 1 in the Appendix.

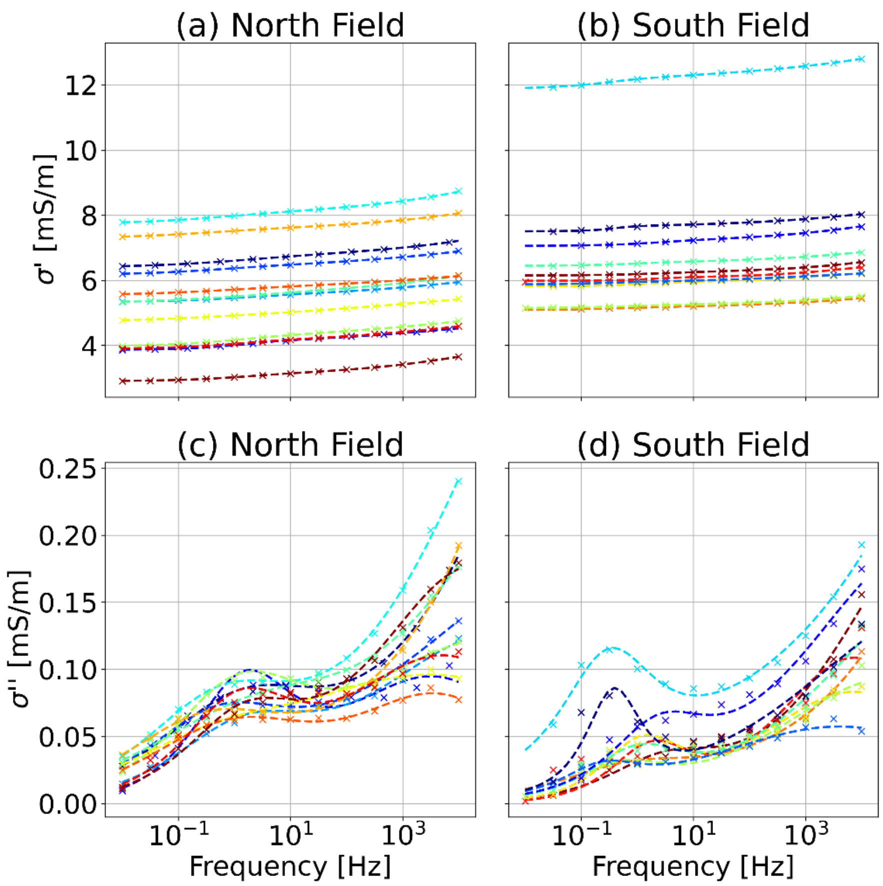

Figure 9: Example of spectra and Pelton model fittings for real conductivity in (a) the North and (b) the South Fields, and imaginary conductivity in (c) the North and (d) the South Fields. Crosses represent data and dashed lines represent Pelton model fits.

The SIP data from the South Field displays an increasing σ' and σ'' towards the southeast (Figures 10b and d). In comparison, data from the North Field displays anomalous patterns in the same location as the anomalous zone identified in Figures 7 and 8 (Figures 10a and c). However, it should be noted that samples with anomalously low σ' are not characterized by anomalous σ'' values. Furthermore, although the σ'' and M_n values have similar patterns, there are some notable differences in the North Field (Figures 10c and e). For instance, the high σ'' anomaly is north of the high M_n anomaly. In comparison, the σ'' and M_n values in the South Field have similar spatial patterns (Figures 10d and f).

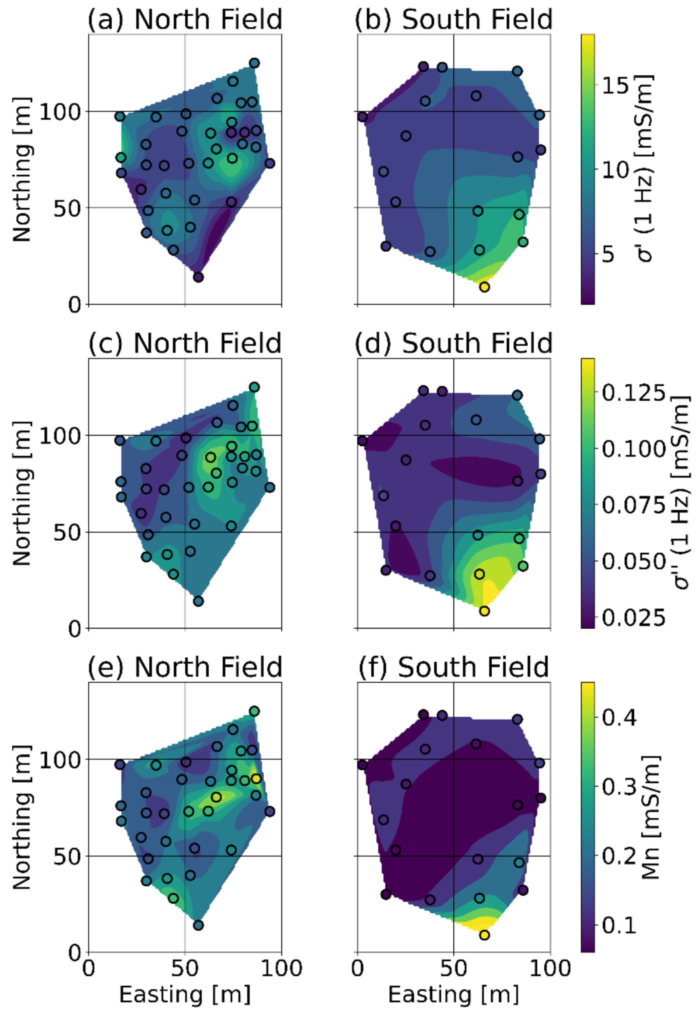

Figure 10: Maps of real conductivity in (a) the North Field and (b) the South Field, imaginary conductivity in (c) the North Field and (d) the South Field, and normalized chargeability in (e) the North Field and (f) the South Field.

607

4.5. Polarization and CEC

The relationships of σ'' and M_n with CEC are shown in Figure 11. Additionally, the plots are colored by the percentage of fine materials (i.e., clay and silt). The CEC values (and the percentage of clay and silt) from each sample interval are presented; doing so allows for the soil intervals with anomalous MS values (see Figure 8) to be highlighted (with red circles). It was anticipated that a positive correlation between polarization and CEC would be observed. However, in the North Field higher σ'' and M_n values are typically associated with lower CEC values, particularly in the top two soil intervals (Figures 10a, b, d, and e). For the North Field, σ'' and CEC values have Spearman correlations of -0.65, -0.60, and -0.42 for each soil interval, respectively.

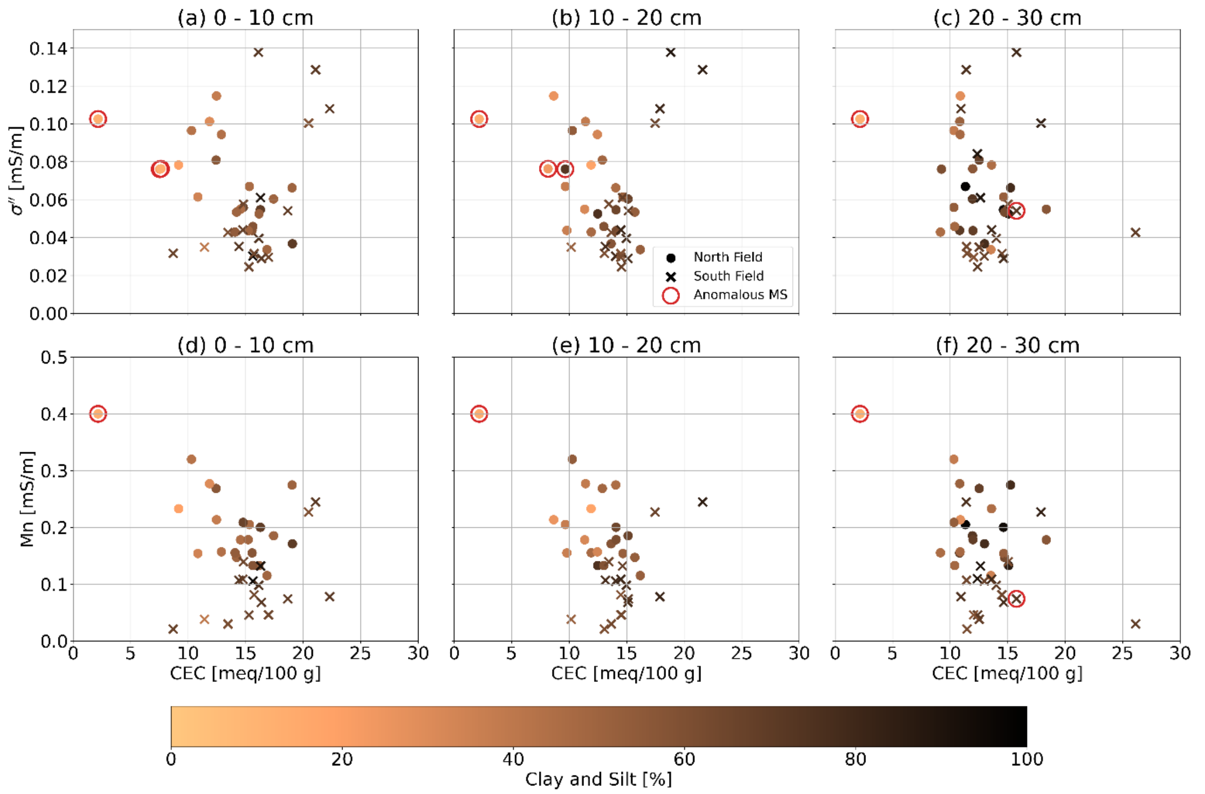

Figure 11: Relationships of CEC and vs polarization for each soil interval in both fields. (a) to (c) show the relationships between CEC and σ'', at 1 Hz, for the 0 – 10, 10 – 20, and 20 – 30 cm intervals. (d) to (f) show the relationships between CEC and M_n for the 0 – 10, 10 – 20, and 20 – 30 cm intervals. Red circles are used to denote soils with anomalous MS values (as identified in Figure 8).

In the South Field, higher σ'' and M_n values are associated with higher CEC values in the top two soil intervals (Figures 10a, b, d, and e). For instance, σ'' and CEC have Spearman correlations of 0.62, and 0.84, for the soil intervals 0 – 10 cm, and 10 – 20 cm, whereas the values for the 20 – 30 cm interval have a correlation of 0.00.

It can be observed that the North Field samples with anomalous magnetic susceptibility values (red circles in Figure 11) are associated with low CEC values. Importantly, even if these samples are removed, the negative correlation between CEC and polarizability still remains, albeit at a weaker level. However, it should be noted that samples from the North Field, where clay and percentages exceed 50%, show broad agreement with the polarization vs. CEC patterns of the South Field data. This implies that mineralogy does influences the polarizability, and it is strongly linked to grain size. Further MS analysis could focus on the sand-rich and sand-poor fractions independently, to assess if the finer-grained soils in the North Field have a comparable MS signature to the South Field soils.

4.6. Prediction of CEC from SIP measurements

Given the anomalous behavior of the coarser North Field samples, this section focuses on North Field samples with a sand content < 50% and the South Field samples. As noted in section 3.3, the fitting parameters for eq. 9 and 10 were determined using the measured CEC and VMC for each site and average porosity values for both fields.

In the South Field the average porosity (61.0%) was used, for the remaining North Field samples the porosity values from the excluded areas were not considered and the average porosity was determined to be 65.7%.

The saturation and cementation exponents were both assumed to be 2 (e.g., Glover et al., 2015).

The fitting coefficients b_{im} and M_n were determined by minimizing the RMSE between the measured and predicted CEC. This approach resulted in $\sigma''(1\,Hz) = 0.013\,\phi S^2 CEC$ and $M_n = 4.41 \times 10^{-5}\,\phi S^2 CEC$ for the North Field samples, and $\sigma''(1\,Hz) = 0.021\,\phi S^2 CEC$ and $M_n = 5.01 \times 10^{-5}\,\phi S^2 CEC$ for the South Field, see Figure 12. The resultant RMSE values for both approaches in the North Field were 3.34 meq/100 g (24.6%) and 3.47 meq/100 g (25.2%), respectively. In comparison, in the South Field the RMSE values were 3.59 meq/100 g (25.6%) and 5.47 meq/100 g (36.9%).

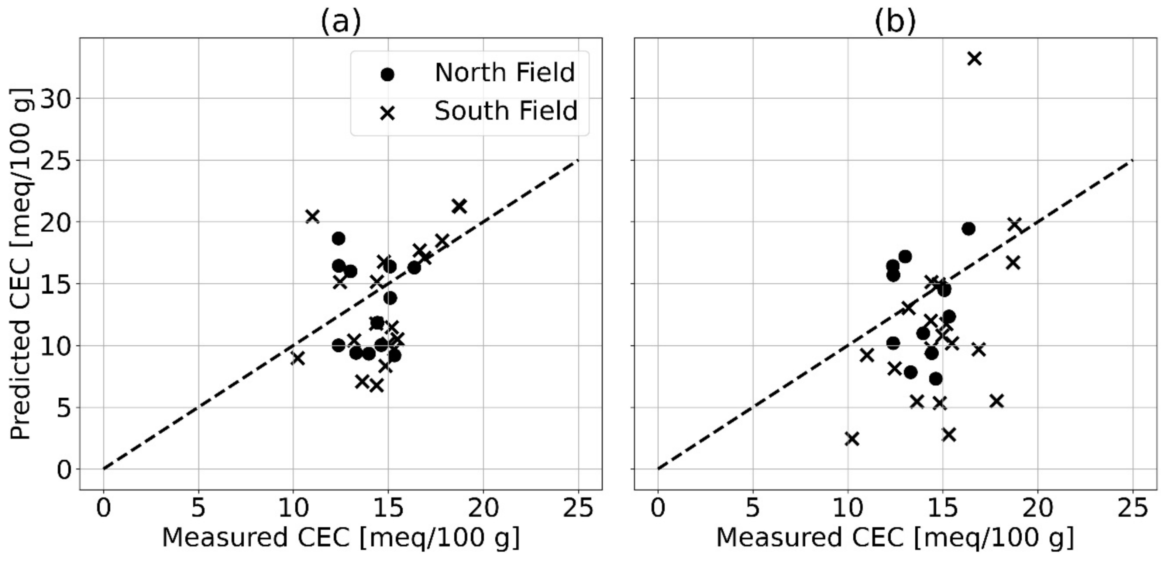

Figure 12: Plot showing the prediction of CEC from (a) σ'' (1 Hz) and (b) M_n, dashed line shows 1:1. As discussed in section 4.6, North Field data with > 50% sand content are omitted.

Importantly, the included North Field data do not form a trend between predicted and measured CEC. This suggests that variability in other soil parameters (e.g., mineralogy, porosity, porewater electrical conductivity) is obscuring the relation between CEC and polarization. In comparison, many of the South Field data lie parallel to the 1:1 line indicating that assumption of homogenous porosities, cementation and saturation exponents, and pore water conductivities is somewhat valid for these samples.

5. Discussion

This work aimed to tackle three principal goals: (1) assessing the advantages of multi-frequency over single-frequency polarization measurements, (2) determining the importance of other parameters in polarization of soils, and (3) evaluating the ability of field-based IP measurements to provide quantitative estimates of CEC.

5.1 Multi-frequency and single-frequency measurements

Although approximations to estimate M_n in limited bandwidth data exist, e.g., Revil et al. (2021), the most accurate characterization of M_n requires collection of broadband SIP data. However, it was evident in this work that M_n values from the Pelton model provided no clear advantage over 1 Hz σ''. Consequently, in many cases, high quality single-frequency IP measurements, may be sufficient for defining the polarization characteristics in soils.

Such conclusions align with the laboratory work of Weller et al. (2010), who observed that predictions of S_{por} from σ'' and M_n were broadly comparable for a range of sands and sandstones. Consequently, it is of more interest to dedicate time to characterizing heterogeneity in space rather than frequency in field cases. For instance, Moser et al. (2023) noted the benefits of 3D IP surveys in landfill characterization in specific comparison to multi-frequency characterization.

However, it should be noted that the correlation between σ'' and sensitivity averaged CEC was the strongest for measurements made at 0.316 Hz in the South Field. Nonetheless, the 1 Hz σ'' exhibited only a slightly weaker correlation with sensitivity averaged CEC.

5.2 The importance of other soil parameters in the polarization signature

Although σ'' is less dependent on VMC than σ' (e.g., Vinegar and Waxman, 1984), inclusion of VMC data in the petrophysical modeling substantially improved the accuracy of CEC predictions. Consequently, it is important to obtain accurate estimates of VMC for such predictions of CEC with IP data. Given the experimental set up of this work, accounting for VMC was relatively straightforward; however in IP tomography it may be unfeasible to measure VMC directly. One could envisage this being problematic in areas with thick unsaturated zones.

Revil et al. (2021) proposed that VMC could be estimated from their approximated M_n and an assumed pore water conductivity. However, given that they use M_n to obtain CEC, as shown in eq. 10, their predictions of CEC are highly susceptible to errors in their M_n values.

In the current work, porosity, cementation and saturation exponents, and pore fluid chemistry were assumed homogenous in each field. It is anticipated that variation in these parameters could contribute to the scatter in the CEC predictions shown in Figure 12a. The importance of these parameters is well documented, e.g., Vinegar and Waxman (1984); however, it should be noted that accurate determination of such properties is comparable in effort to direct measurement of CEC.

One possible route to separate surface conductivity and electrolytic conductivity, and therefore estimate both saturation and porewater electrical conductivity, could be via the proportionality factor ($l = \sigma''/\sigma'_{surf}$), Börner, (1992) and Weller et al. (2013). For instance, Weller et al. (2013) demonstrated that $l = 0.042$ for a database of sandstones and unconsolidated sediments. In the North Field, there was a negligible correlation (*Spearman's correlation = 0.07*) between 1 Hz σ' and VMC; which indicates that σ'_{surf} dominates σ'. However, there was only a moderate correlation (*Spearman's correlation = 0.39*) between the 1 Hz σ' and σ'' in the North Field; which indicates that the proportionally factor is variable. In the South Field, given the stronger correlation between 1 Hz σ' and VMC (Spearman's correlation = 0.75), σ' cannot be assumed to be independent from electrolytic conductivity. However, in the absence of detailed information on electrolytic conductivity in the South Field, the nature of the proportionality factor cannot be validated. Future work ought to explore the usefulness of the proportionality factor in IP based predictions of CEC.

From the magnetic susceptibility data, it was interpreted that the mineralogy of the North Field soil is more diverse than the South Field. Peshtani et al. (2022) demonstrated positive linear and power-law relationships between magnetic susceptibility and polarization for a diverse range of sediments. However, in the present work there was a non-monotonic relationship between χLF and σ'' (Figure 13b). For instance, when χLF is < 200×10^{-9} m^3/kg, σ'' varies substantially without a clear relation to χLF in both fields. When χLF is > 200×10^{-9} m^3/kg, there appears to be a weakly positive correlation between χLF and σ'' for the North Field data, and no correlation for the South Field data. It should be noted that the samples in Peshtani et al. (2022) had much stronger magnetic signatures; and that it was observed by Chen et al. (2021) that MS and σ'' were poorly correlated for weakly magnetic serpentinized basalts. Nonetheless, the relationship between imaginary conductivity and magnetic susceptibility has clear importance for CEC prediction in magnetically influenced soils and is worthy of further study.

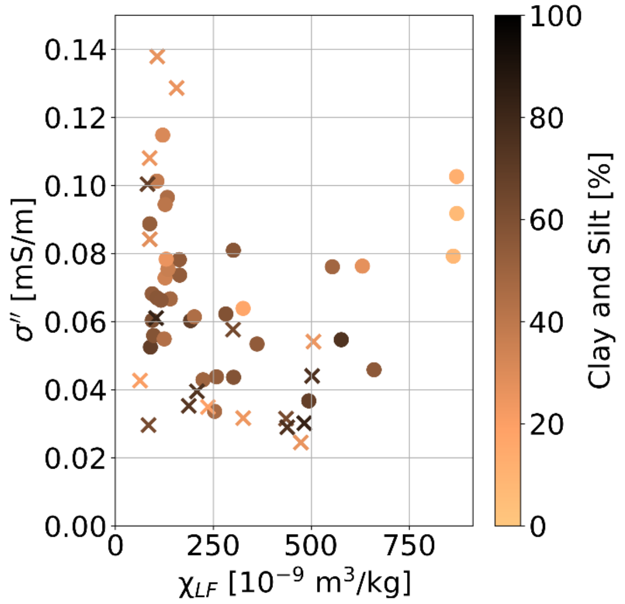

Figure 13: Plot showing the non-monotonic relationship between χ_{LF} and 1 Hz σ''.

5.3 The ability of field-based IP to quantify CEC

The last objective of the work was to assess the ability of field-based IP to quantify CEC. To better visualize the field-based CEC predictions it is useful to plot them alongside the laboratory data from Figure 2. Figure 14 shows predicted vs measured CEC for the South Field data, the North Field data with < 50 % sand content, and the laboratory data. The predicted CEC for the laboratory data assumes a global relationship of $\sigma'' = 0.027\,CEC$. Although one could argue that a better fit of the laboratory samples could be achieved using a separate coefficient for each data set, this allows for a more objective comparison with the field data given that porosities and cementation coefficients were not well-defined.

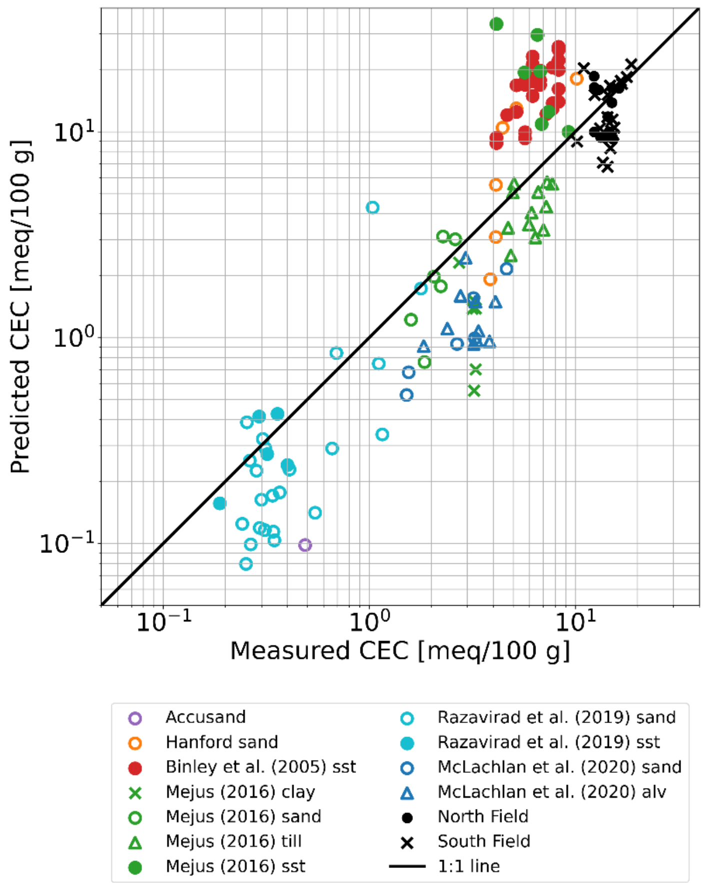

Figure 14: Predicted and measured CEC values for laboratory data from Lancaster University, as shown in Figure 2, and field data, as shown in Figure 12. Sst refers to sandstone samples.

The predictions from the field data lie comparatively close to the 1:1 line, indicating that relatively accurate estimates of CEC could be obtained from IP measurements. For instance, one could envisage building a larger database of field-based IP and CEC data for order-of-magnitude CEC estimates. Although order-of-magnitude estimates ought to be useful in informing nutrient retention in agricultural and hydrogeological systems, it is anticipated that in most cases, CEC will not vary orders of magnitude across the field site. Future work ought to extend the methodology to other field sites, particularly those with non-magnetic soils, to build a larger measurement database.

6. Conclusions

This study addressed three key objectives related to the application of induced polarization (IP) measurements in CEC characterization. First, the investigation into multi-frequency versus single-frequency polarization measurements revealed that single-frequency IP measurements, or time-domain IP measurements, may be sufficient for characterizing polarization characteristics of geological materials.

Second, the study indicated the importance of soil parameters such as moisture content, porosity, pore fluid chemistry, and mineralogy on polarization signatures. Mineralogy was identified to have a significant role, indicating that consideration of soil parent materials and soil management ought to be considered before CEC is estimated with electrical approaches. To assess magnetic influence, one could envisage conducting an EMI survey to identify anomalous regions (e.g., McLachlan et al., 2022).

Given the importance of VMC on polarization signature future work in unsaturated zones ought to consider uncertainty related to VMC. However, it should be noted that IP-based CEC prediction could be more viable in saturated settings. For instance, in cases where the subsurface is saturated (e.g., wetlands, and river and lake beds) one could envisage obtaining more accurate CEC predictions without the need for VMC measurements. The CEC values of sediments here are important as they govern the transfer of nutrients and pollutants between groundwater and surface water. Moreover, saturated conditions would also allow for an easier constraint on porewater conductivity, which would likely yield improved CEC predictions.

Nonetheless, despite the uncertainties of working in the unsaturated zone, field-based IP measurements demonstrated promising results for quantifying CEC, particularly in the South Field. The derived petrophysical relationship showed broad agreement with the large-scale patterns present in the laboratory measurements for data in both the North and South Field.

Overall, this work contributes valuable insights into the complexities of utilizing IP measurements for CEC characterization. The findings provide a foundation for future research to refine and expand the applicability of field-based IP measurements in diverse settings.

7. References

Abdelwaheb, Mohamed, Khaoula Jebali, Hatem Dhaouadi, and Sonia Dridi-Dhaouadi. "Adsorption of Nitrate, Phosphate, Nickel and Lead on Soils: Risk of Groundwater Contamination." *Ecotoxicology and Environmental Safety* 179 (September 2019): 182–87. https://doi.org/10.1016/j.ecoenv.2019.04.040.

Archie, G.E. “The Electrical Resistivity Log as an Aid in Determining Some Reservoir Characteristics.” *Transactions of the AIME* 146, no. 01 (December 1, 1942): 54–62. https://doi.org/10.2118/942054-G.

Binley, Andrew, Lee D. Slater, Melanie Fukes, and Giorgio Cassiani. “Relationship between Spectral Induced Polarization and Hydraulic Properties of Saturated and Unsaturated Sandstone.” *Water Resources Research* 41, no. 12 (December 2005): 2005WR004202. https://doi.org/10.1029/2005WR004202.

Cole, Kenneth S., and Robert H. Cole. “Dispersion and Absorption in Dielectrics I. Alternating Current Characteristics.” *The Journal of Chemical Physics* 9, no. 4 (April 1, 1941): 341–51. https://doi.org/10.1063/1.1750906.

Chen, H., Tao, C., Revil, A., Zhu, Z., Zhou, J., Wu, T., & Deng, X. “Induced polarization and magnetic responses of serpentinized ultramafic rocks from mid-ocean ridges.” Journal of Geophysical Research: Solid Earth, (2012) 126, e2021JB022915. https://doi.org/10.1029/2021JB022915

Du Laing, G., J. Rinklebe, B. Vandecasteele, E. Meers, and F.M.G. Tack. “Trace Metal Behaviour in Estuarine and Riverine Floodplain Soils and Sediments: A Review.” *Science of The Total Environment* 407, no. 13 (June 2009): 3972–85. https://doi.org/10.1016/j.scitotenv.2008.07.025.

Gaines T. P., Gaines, S. T. (1994) Soil texture effect on nitrate leaching in soil percolates, Communications in Soil Science and Plant Analysis, 25:13-14, 2561-2570, DOI: 10.1080/00103629409369207

Glover P.W.J Geophysical Properties of the Near Surface Earth: Electrical Properties. In: Gerald Schubert (editor-in-chief) Treatise on Geophysics, 2nd edition, Vol 11. Oxford: Elsevier; 2015. p. 89-137.

Flores Orozco, Adrián, Matthias Bücker, Matthias Steiner, and Jean-Philippe Malet. "Complex-Conductivity Imaging for the Understanding of Landslide Architecture." *Engineering Geology* 243 (September 2018): 241–52. https://doi.org/10.1016/j.enggeo.2018.07.009.

Jougnot, D., A. Ghorbani, A. Revil, P. Leroy, and P. Cosenza. "Spectral Induced Polarization of Partially Saturated Clay-Rocks: A Mechanistic Approach." *Geophysical Journal International* 180, no. 1 (January 2010): 210–24. https://doi.org/10.1111/j.1365-246X.2009.04426.x.

Kemna, Andreas, Andrew Binley, Giorgio Cassiani, Ernst Niederleithinger, André Revil, Lee Slater, Kenneth H. Williams, et al. "An Overview of the Spectral Induced Polarization Method for Near-surface Applications." *Near Surface Geophysics* 10, no. 6 (December 2012): 453–68. https://doi.org/10.3997/1873-0604.2012027.

McLachlan, P., J. Chambers, S. Uhlemann, and A. Binley. "Limitations and Considerations for Electrical Resistivity and Induced Polarization Imaging of Riverbed Sediments: Observations from Laboratory, Field, and Synthetic Experiments." *Journal of Applied Geophysics* 183 (December 2020): 104173. https://doi.org/10.1016/j.jappgeo.2020.104173.

McLachlan, P., M. Schmutz, J. Cavailhes, and S.S. Hubbard. "Estimating Grapevine-Relevant Physicochemical Soil Zones Using Apparent Electrical Conductivity and in-Phase Data from EMI Methods." *Geoderma* 426 (November 2022): 116033. https://doi.org/10.1016/j.geoderma.2022.116033.

Niu, Q., Prasad, M., Revil, A. and Saidian, M., 2016. Textural control on the quadrature conductivity of porous media. Geophysics, 81(5), pp.E297-E309.

Moser, Clemens, Andrew Binley, and Adrian Flores Orozco. "3D Electrode Configurations for Spectral Induced Polarization Surveys of Landfills." *Waste Management* 169 (September 2023): 208–22. https://doi.org/10.1016/j.wasman.2023.07.006.

Overton, Kathy, Tim Dempster, Stephen E. Swearer, Rebecca L. Morris, and Luke T. Barrett. "Achieving Conservation and Restoration Outcomes through Ecologically Beneficial Aquaculture." *Conservation Biology*, February 21, 2023, e14065. https://doi.org/10.1111/cobi.14065.

Pelton, W. H., S. H. Ward, P. G. Hallof, W. R. Sill, and P. H. Nelson. "MINERAL DISCRIMINATION AND REMOVAL OF INDUCTIVE COUPLING

WITH MULTIFREQUENCY IP.” *GEOPHYSICS* 43, no. 3 (April 1978): 588–609. https://doi.org/10.1190/1.1440839.

Peshtani, K., Weller, A., Saneiyan, S. and Slater, L., 2022. The influence of magnetic minerals on induced polarization measurements in sedimentary rocks. Geophysical Research Letters, 49(19), p.e2022GL100192.

Razavirad, Fatemeh, Myriam Schmutz, and Andrew Binley. “Estimation of the Permeability of Hydrocarbon Reservoir Samples Using Induced Polarization and Nuclear Magnetic Resonance Methods.” *GEOPHYSICS* 84, no. 2 (March 1, 2019): MR73–84. https://doi.org/10.1190/geo2017-0745.1.

Revil, A. “Effective Conductivity and Permittivity of Unsaturated Porous Materials in the Frequency Range 1 MHz–1GHz.” *Water Resources Research* 49, no. 1 (January 2013): 306–27. https://doi.org/10.1029/2012WR012700.

Revil, A. “Spectral Induced Polarization of Shaly Sands: Influence of the Electrical Double Layer.” *Water Resources Research* 48, no. 2 (February 2012): 2011WR011260. https://doi.org/10.1029/2011WR011260.

Revil, A., and N. Florsch. “Determination of Permeability from Spectral Induced Polarization in Granular Media.” *Geophysical Journal*

International, March 2010. https://doi.org/10.1111/j.1365-246X.2010.04573.x.

Revil, A., Coperey, A., Shao, Z., Florsch, N., Fabricius, I. L., Deng, Y., Delsman, J., Pauw, P., Karaoulis, M., de Louw, P. G. B., van Baaren, E. S., Dabekaussen, W., Menkovic, A., & Gunnink, J. L. (2017). “Complex conductivity of soils.” *Water Resources Research*, 53(8), (2017). https://doi.org/10.1002/2017WR020655

Revil, A., M. Schmutz, F. Abdulsamad, A. Balde, C. Beck, A. Ghorbani, and S.S. Hubbard. “Field-Scale Estimation of Soil Properties from Spectral Induced Polarization Tomography.” *Geoderma* 403 (December 2021): 115380. https://doi.org/10.1016/j.geoderma.2021.115380.

Revil, André, Pierre Vaudelet, Zhaoyang Su, and Rujun Chen. “Induced Polarization as a Tool to Assess Mineral Deposits: A Review.” *Minerals* 12, no. 5 (April 30, 2022): 571. https://doi.org/10.3390/min12050571.

Schmutz, Myriam, Ahmad Ghorbani, Pierre Vaudelet, and Amélie Blondel. “Cable Arrangement to Reduce Electromagnetic Coupling Effects in Spectral-Induced Polarization Studies.” *GEOPHYSICS* 79, no. 2 (March 1, 2014): A1–5. https://doi.org/10.1190/geo2013-0301.1.

Singha, K., F. D. Day-Lewis, T. Johnson, and L. D. Slater. “Advances in Interpretation of Subsurface Processes with Time-lapse Electrical

Imaging." *Hydrological Processes* 29, no. 6 (March 15, 2015): 1549–76. https://doi.org/10.1002/hyp.10280.

Slater, Lee. "Near Surface Electrical Characterization of Hydraulic Conductivity: From Petrophysical Properties to Aquifer Geometries—A Review." *Surveys in Geophysics* 28, no. 2–3 (September 11, 2007): 169–97. https://doi.org/10.1007/s10712-007-9022-y.

Smith, J.W.N., and D.N. Lerner. "Geomorphologic Control on Pollutant Retardation at the Groundwater-Surface Water Interface." *Hydrological Processes* 22, no. 24 (November 30, 2008): 4679–94. https://doi.org/10.1002/hyp.7078.

Tarasov, Andrey, and Konstantin Titov. "On the Use of the Cole–Cole Equations in Spectral Induced Polarization." *Geophysical Journal International* 195, no. 1 (October 1, 2013): 352–56. https://doi.org/10.1093/gji/ggt251.

Triantafilis, John, Scott Mitchell Lesch, Kevin La Lau, and Sam Mostyn Buchanan. "Field Level Digital Soil Mapping of Cation Exchange Capacity Using Electromagnetic Induction and a Hierarchical Spatial Regression Model." *Soil Research* 47, no. 7 (2009): 651. https://doi.org/10.1071/SR08240.

Vinegar, H. J., and M. H. Waxman. "Induced Polarization of Shaly Sands." *GEOPHYSICS* 49, no. 8 (August 1984): 1267–87. https://doi.org/10.1190/1.1441755.

Wait, James R. "Relaxation Phenomena and Induced Polarization." *Geoexploration* 22, no. 2 (April 1984): 107–27. https://doi.org/10.1016/0016-7142(84)90032-2.

Waxman, M.H., and L.J.M. Smits. "Electrical Conductivities in Oil-Bearing Shaly Sands." *Society of Petroleum Engineers Journal* 8, no. 02 (June 1, 1968): 107–22. https://doi.org/10.2118/1863-A.

Weller, A., and L.D. Slater. "Induced Polarization Dependence on Pore Space Geometry: Empirical Observations and Mechanistic Predictions." *Journal of Applied Geophysics* 123 (December 2015): 310–15. https://doi.org/10.1016/j.jappgeo.2015.09.002.

Weller, Andreas, and Lee Slater. "Induced Polarization Dependence on Pore Space Geometry: Empirical Observations and Mechanistic Predictions." *Journal of Applied Geophysics* 123 (December 2015): 310–15. https://doi.org/10.1016/j.jappgeo.2015.09.002.

Weller, Andreas, and Lee Slater. "Ambiguity in Induced Polarization Time Constants and the Advantage of the Pelton Model." *GEOPHYSICS* 87, no. 6 (November 1, 2022): E393–99. https://doi.org/10.1190/geo2022-0158.1.

Weller, Andreas, Lee Slater, and Sven Nordsiek. "On the Relationship between Induced Polarization and Surface Conductivity: Implications for Petrophysical Interpretation of Electrical Measurements."

GEOPHYSICS 78, no. 5 (September 1, 2013): D315–25. https://doi.org/10.1190/geo2013-0076.1.

Weller, Andreas, and Lee Slater. "Permeability Estimation from Induced Polarization: An Evaluation of Geophysical Length Scales Using an Effective Hydraulic Radius Concept." *Near Surface Geophysics* 17, no. 6 (December 2019): 581–94. https://doi.org/10.1002/nsg.12071.

Weller, Andreas, Lee Slater, Sven Nordsiek, and Dimitrios Ntarlagiannis. "On the Estimation of Specific Surface per Unit Pore Volume from Induced Polarization: A Robust Empirical Relation Fits Multiple Data Sets." *GEOPHYSICS* 75, no. 4 (July 2010): WA105–12. https://doi.org/10.1190/1.3471577.

Zimmermann, E, A Kemna, J Berwix, W Glaas, and H Vereecken. "EIT Measurement System with High Phase Accuracy for the Imaging of Spectral Induced Polarization Properties of Soils and Sediments." *Measurement Science and Technology* 19, no. 9 (September 1, 2008): 094010. https://doi.org/10.1088/0957-0233/19/9/094010.

Dearing, J. A. *Environmental Magnetic Susceptibility: Using the Bartington MS2 System*. Kenilworth: Chi Pub., 1994.

Dearing, J. A., R. J. L. Dann, K. Hay, J. A. Lees, P. J. Loveland, B. A. Maher, and K. O'Grady. "Frequency-Dependent Susceptibility Measurements of Environmental Materials." *Geophysical Journal*

International 124, no. 1 (January 1996): 228–40. https://doi.org/10.1111/j.1365-246X.1996.tb06366.x.

Grimley, D. A., and M. J. Vepraskas. "Magnetic Susceptibility for Use in Delineating Hydric Soils." *Soil Science Society of America Journal* 64, no. 6 (November 2000): 2174–80. https://doi.org/10.2136/sssaj2000.6462174x.

Grimley, David A., Jing-Shu Wang, Derek A. Liebert, and Jeffrey O. Dawson. "Soil Magnetic Susceptibility: A Quantitative Proxy of Soil Drainage for Use in Ecological Restoration." *Restoration Ecology* 16, no. 4 (December 2008): 657–67. https://doi.org/10.1111/j.1526-100X.2008.00479.x.

Maher, Barbara A. "Magnetic Properties of Some Synthetic Sub-Micron Magnetites." *Geophysical Journal International* 94, no. 1 (July 1988): 83–96. https://doi.org/10.1111/j.1365-246X.1988.tb03429.x.

9. Appendix

Table 1: A summary of the samples and key data for the samples in this work. Sites with names starting 'N' denote North Field, and sites with names starting 'S' denote South Field. The σ' RMSE and σ'' RMSE denote the root-mean-square-error of the double Pelton model fitting.

Site Name	1 Hz σ' (mS/m)	1 Hz σ'' (mS/m)	ρ_0 (ohm.m)	M_n (mS/m)	σ' RMSE (%)	σ'' RMSE (%)
NP1	6.577	0.078	156.528	0.331	0.040	2.760
NP2	3.984	0.079	258.617	0.270	0.210	14.350
NP3	6.371	0.074	162.593	0.225	0.050	1.770
NP4	5.463	0.060	187.778	0.217	0.060	5.420
NP5	7.979	0.089	129.454	0.325	0.070	1.620
NP6	5.498	0.073	189.585	0.426	0.100	3.970
NP7	4.174	0.092	252.532	0.319	0.140	3.540
NP8	4.921	0.064	212.089	0.139	0.070	1.910
NP9	7.518	0.068	137.509	0.256	0.040	1.960
NP10	5.719	0.062	180.568	0.310	0.090	2.440
NP11	4.049	0.075	256.517	0.241	0.150	9.760
NP12	3.028	0.067	344.809	0.211	0.140	7.590
NV1	7.836	0.067	129.516	0.205	0.140	10.450
NV2	7.399	0.055	137.010	0.200	0.410	6.370
NV3	5.546	0.044	183.506	0.155	0.460	2.620
NV4	8.272	0.052	122.268	0.133	0.310	8.760
NV5	6.267	0.034	161.107	0.115	0.380	22.530
NV6	10.103	0.115	102.103	0.213	0.500	6.870
NV7	10.224	0.103	66.070	0.400	0.500	6.660
NV8	12.464	0.076	-	-	-	-
NV9	7.388	0.078	11.818	0.233	0.460	16.820
NV10	8.267	0.066	41.262	0.275	0.460	3.050
NV11	8.364	0.056	41.265	0.209	0.400	7.120

NV12	6.800	0.055	27.754	0.178	0.470	10.410
NH1	9.212	0.081	18.558	0.268	0.450	14.690
NH2	6.965	0.053	30.344	0.147	0.440	5.180
NH3	3.905	0.037	65.565	0.171	0.530	4.930
NH4	11.613	0.060	19.501	0.185	0.300	26.020
NH5	5.780	0.043	34.747	0.155	0.420	6.210
NH6	5.019	0.046	15.289	0.133	0.470	26.810
NH7	6.808	0.061	25.990	0.154	0.440	8.220
NH8	9.967	0.096	17.666	0.320	0.450	7.270
NH9	6.158	0.044	57.415	0.178	0.420	1.420
NH10	9.738	0.101	10.930	0.277	0.490	18.020
NH11	7.761	0.076	-	-	-	-
NH12	7.730	0.094	18.101	0.157	0.570	8.030
SH1	3.498	0.035	2.277	0.038	4.500	62.460
SH2	3.470	0.024	7.152	0.046	2.360	67.790
SH3	4.470	0.032	0.661	0.021	3.380	71.090
SH4	9.934	0.084	0.890	0.110	1.010	57.620
SH5	5.293	0.054	1.317	0.074	3.330	59.880
SH6	4.679	0.043	0.675	0.030	1.840	36.980
SH7	12.126	0.108	2.219	0.078	1.990	72.800
SH8	10.933	0.129	2.123	0.245	2.060	67.840
SH9	18.232	0.138	23.078	0.627	1.160	47.690
SV1	6.196	0.030	32.122	0.105	0.100	11.710
SV2	6.035	0.035	14.124	0.107	0.260	32.650
SV3	5.161	0.031	8.784	0.081	0.060	4.690

SV4	5.892	0.044	9.574	0.109	0.180	16.420
SV5	5.212	0.029	4.371	0.068	0.100	13.480
SV6	6.521	0.039	8.500	0.098	0.110	12.400
SV7	12.176	0.100	2.529	0.227	0.040	4.430
SV8	5.947	0.030	1.768	0.046	0.100	4.570
SV9	7.134	0.058	21.151	0.139	0.090	9.610
SV10	7.651	0.061	2.314	0.132	0.140	13.580